Supporting Information

Chromium-rich $Cr_xIr_{1-x}O_2$ Wire-in-tube Alloys for Boosted Water Oxidation with Long Standing Electrocatalytic Activity

Dasol Jin[1,a], *Jisoo Kang*[1,a], *Sampath Prabhakaran*[2,a], *Youngmi Lee*[1], *Myung Hwa Kim*[1,*], *Do Hwan Kim*[3,*] *and Chongmok Lee*[1,*]

[1] Department of Chemistry & Nanoscience, Ewha Womans University, Seoul 03760, Korea

[2] Department of Nano Convergence Engineering, Jeonbuk National University, Jeonbuk 54896, Korea.

[3] Division of Science Education and Institute of Fusion Science, Graduate School of Department of Energy Storage / Energy Conversion Engineering, Jeonbuk National University, Jeonbuk 54896, Jeonbuk, Korea

[a]Authors equally contributed to this work.

*Correspondence:
myungkim@ewha.ac.kr (M.H.K.), dhk201@jbnu.ac.kr (D.H.K), cmlee@ewha.ac.kr (C.L.)

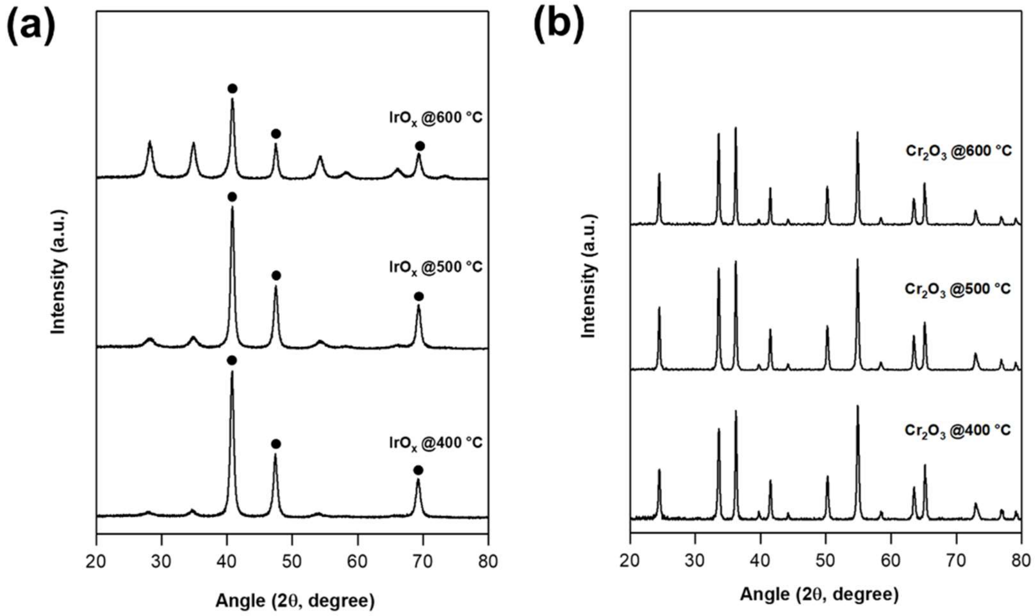

Fig. S1. XRD patterns of pure metal oxides (*i.e.,* IrO$_x$ or Cr_2O_3) synthesized at different calcination temperatures (400 °C, 500 °C and 600 °C). The peaks marked with ● are the XRD peaks of Ir(0) whereas the unmarked peaks are the XRD peaks of IrO_2 in (a) and Cr_2O_3 in (b), respectively.

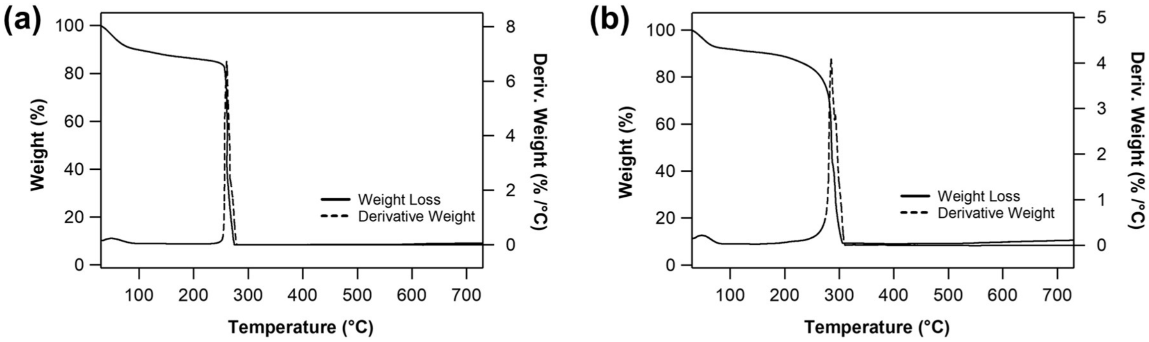

Fig. S2. Thermogravimetric analysis (TGA) curves of (a) $CrCl_3$+$IrCl_3$/PVP as-spun and (b) $IrCl_3$/PVP as-spun.

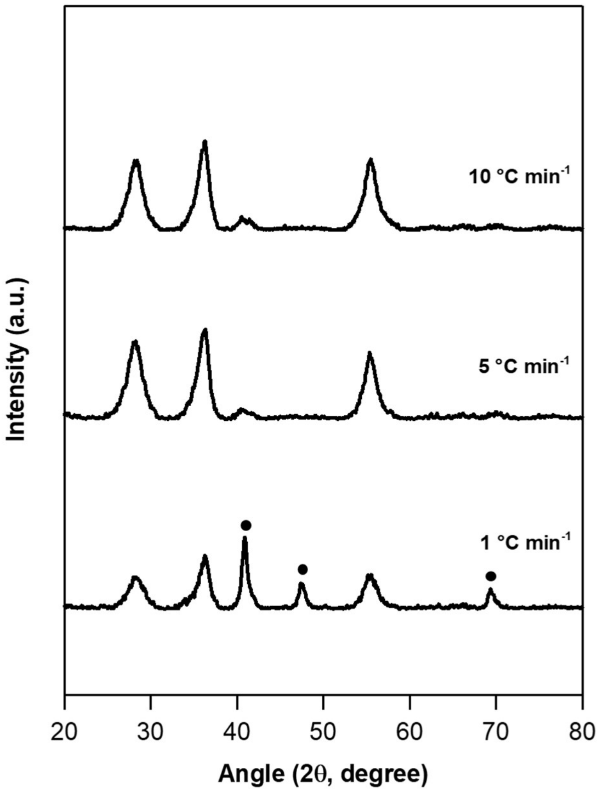

Fig. S3. XRD patterns of Cr-Ir binary metal nanostructures synthesized at 400 °C with heat-treatment rate (1, 5 and 10 °C min^{-1}), respectively. The peaks marked with ● are the XRD peaks of Ir(0) whereas the unmarked peaks are the XRD peaks of IrO_2. Note, the sample annealed at a rate of 5 °C min^{-1} is identical with core-shell $Cr_xIr_{1-x}O_2$ @400 °C.

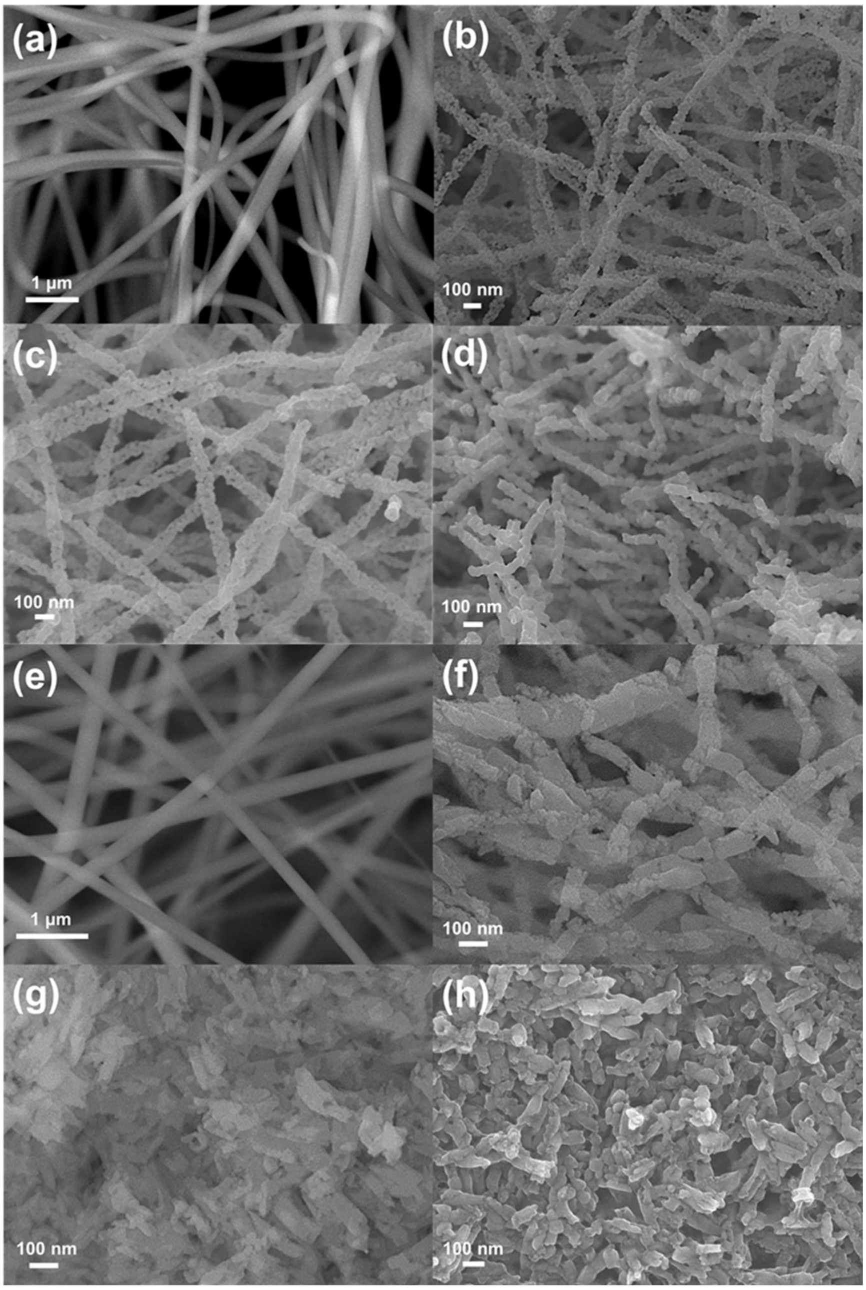

Fig. S4. SEM images of (a-d) single Ir component and (e-f) single Cr component electrospun: (a) $IrCl_3$/PVP, (b) IrO_x @400 °C, (c) IrO_x @500 °C, (d) IrO_x @600 °C, (e) $CrCl_3$/PVP, (f) Cr_2O_3 @400 °C, (g) Cr_2O_3 @500 °C and (h) Cr_2O_3 @600 °C. Note that the SEM image for (h) is the result of applying 1.0 nm Pt-coating to the nanomaterial surface subsidiarily.

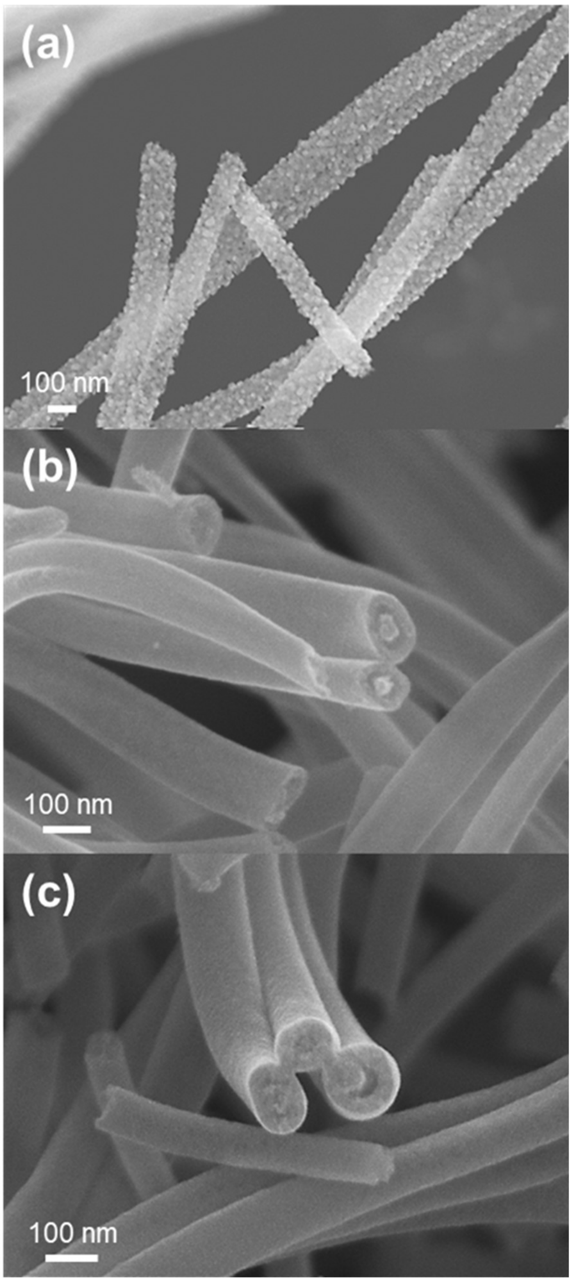

Fig. S5. SEM images of Cr-Ir binary metal oxide alloys with different annealing rate conditions (corresponding to Fig. S3): (a) for 1 °C min^{-1}, (b) for 5 °C min^{-1} and (c) for 10 °C min^{-1}, respectively. Note, the sample annealed at a rate of 5 °C min^{-1} is identical with wire-in-tube nanostructured $Cr_xIr_{1-x}O_2$ @400 °C.

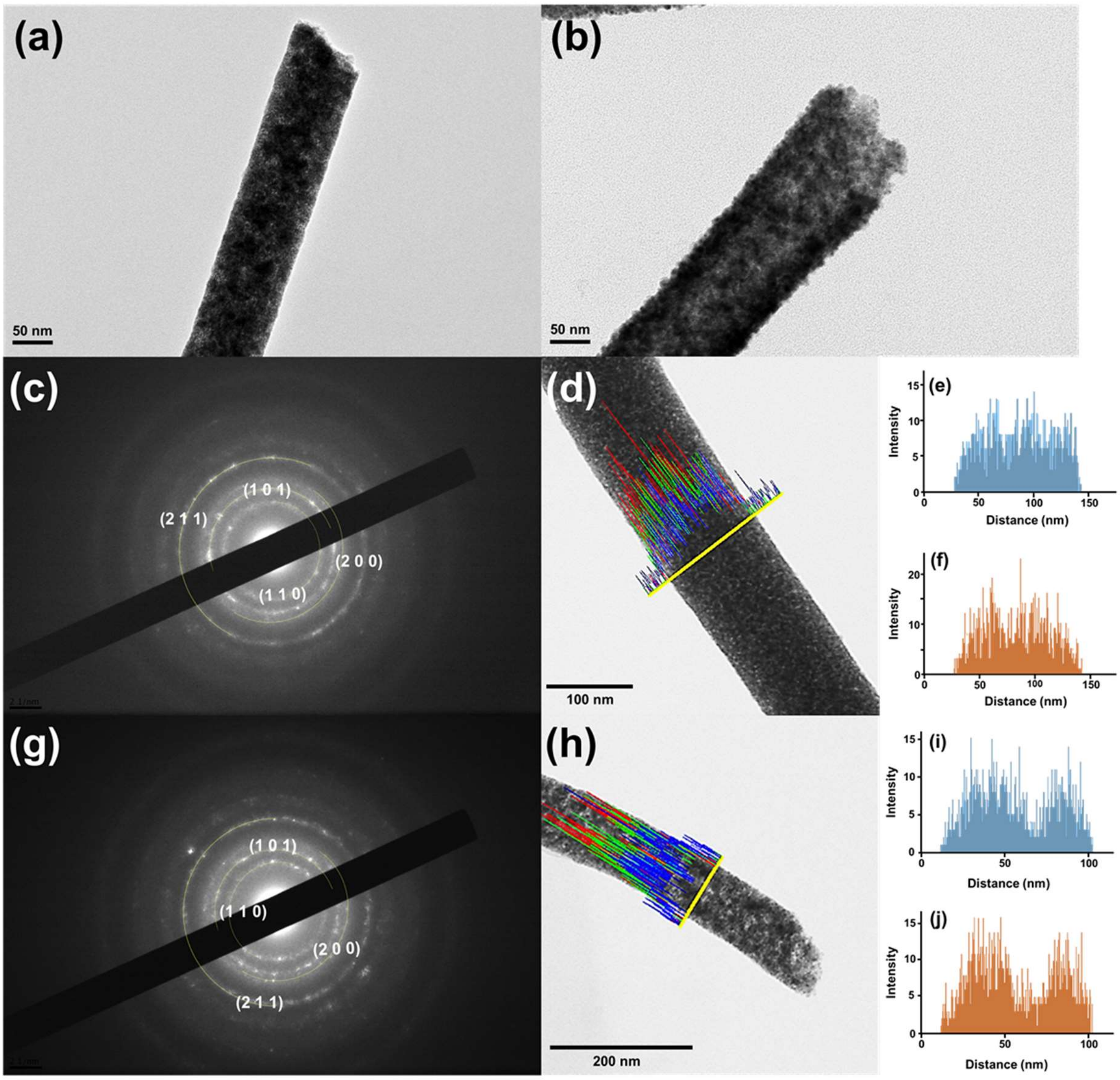

Fig. S6. Low-magnification TEM images of Cr-Ir binary metal oxide alloy with annealing speed of (a) 1 °C min^{-1} and (b) 10 °C min^{-1}. (c) SAED pattern of corresponding to (a). (d) cross-sectional EDS elemental mapping of samples annealed with 1 °C min^{-1} for (g) iridium and (h) chromium. (g) SAED pattern of corresponding to (b). (h) cross-sectional EDS elemental mapping of samples annealed with 10 °C min^{-1} for (i) iridium and (j) chromium.

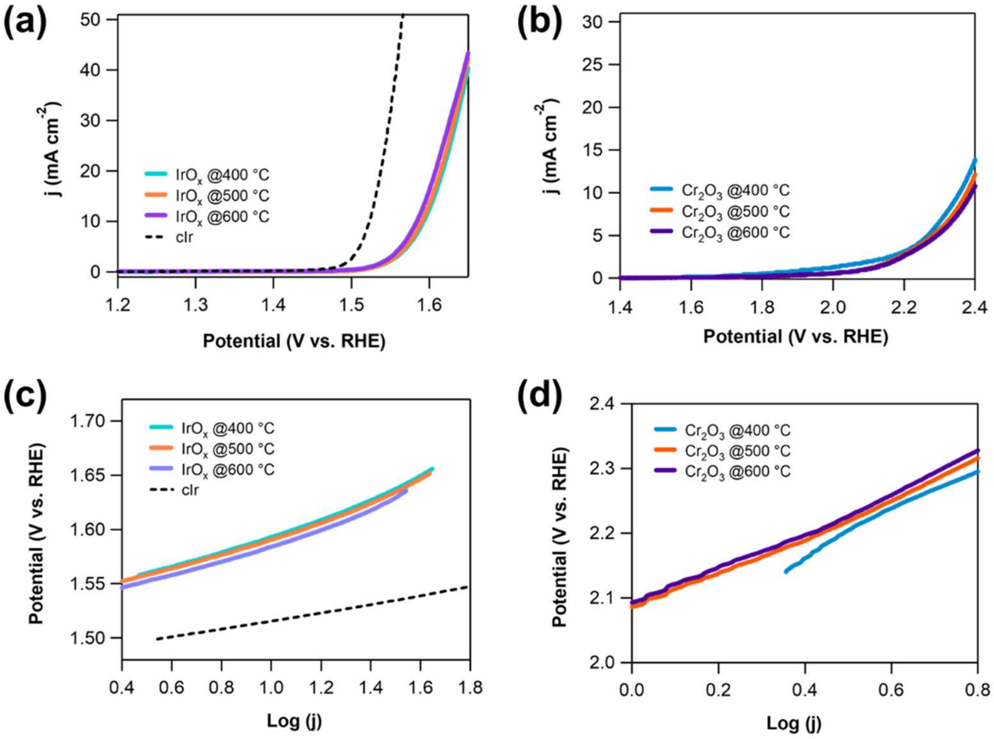

Fig. S7. Comparison of the OER activities of pure metal oxides synthesized at different calcination temperatures (400, 500 and 600 °C): RDE polarization curves of (a) IrO_x and (b) Cr_2O_3, and Tafel slopes of (c) IrO_x and (d) Cr_2O_3. The Tafel slopes obtained from the voltammograms shown in (a) and (b) were derived from the LSVs recorded at 1 mV s^{-1}.

Table S1. Comparison of the Tafel slopes and potentials corresponding to 10 mA cm^{-2} for the synthesized nanomaterials and cIr in 1.0 M KOH (*aq*) solution.

Catalyst	**Potential @ 10 mA cm^{-2} (V *vs*. RHE)**	**Tafel slope (mV dec^{-1})**
[a]$Cr_xIr_{1-x}O_2$ @400 °C	1.510	39.3
$Cr_xIr_{1-x}O_2$ @500 °C	1.569	49.9
$Cr_xIr_{1-x}O_2$ @600 °C	1.584	60.2
[b]$Cr_xIr_{1-x}O_2$ (1 °C min^{-1})	1.514	49.3
[c]$Cr_xIr_{1-x}O_2$ (10 °C min^{-1})	1.534	53.7
IrO_x @400 °C	1.591	78.4
IrO_x @500 °C	1.593	76.6
IrO_x @600 °C	1.591	68.5
Cr_2O_3 @400 °C	2.356	316.9
Cr_2O_3 @500 °C	2.376	293.8
Cr_2O_3 @600 °C	2.391	306.0
cIr	1.523	47.9

[a]Cr-Ir binary metal oxides synthesized at 400 °C with ramping speed of 5 °C min^{-1}. [b]Cr-Ir binary metal oxides synthesized at 400 °C with ramping speed of 1 °C min^{-1}. [c]Cr-Ir binary metal oxides synthesized at 400 °C with ramping speed of 10 °C min^{-1}.

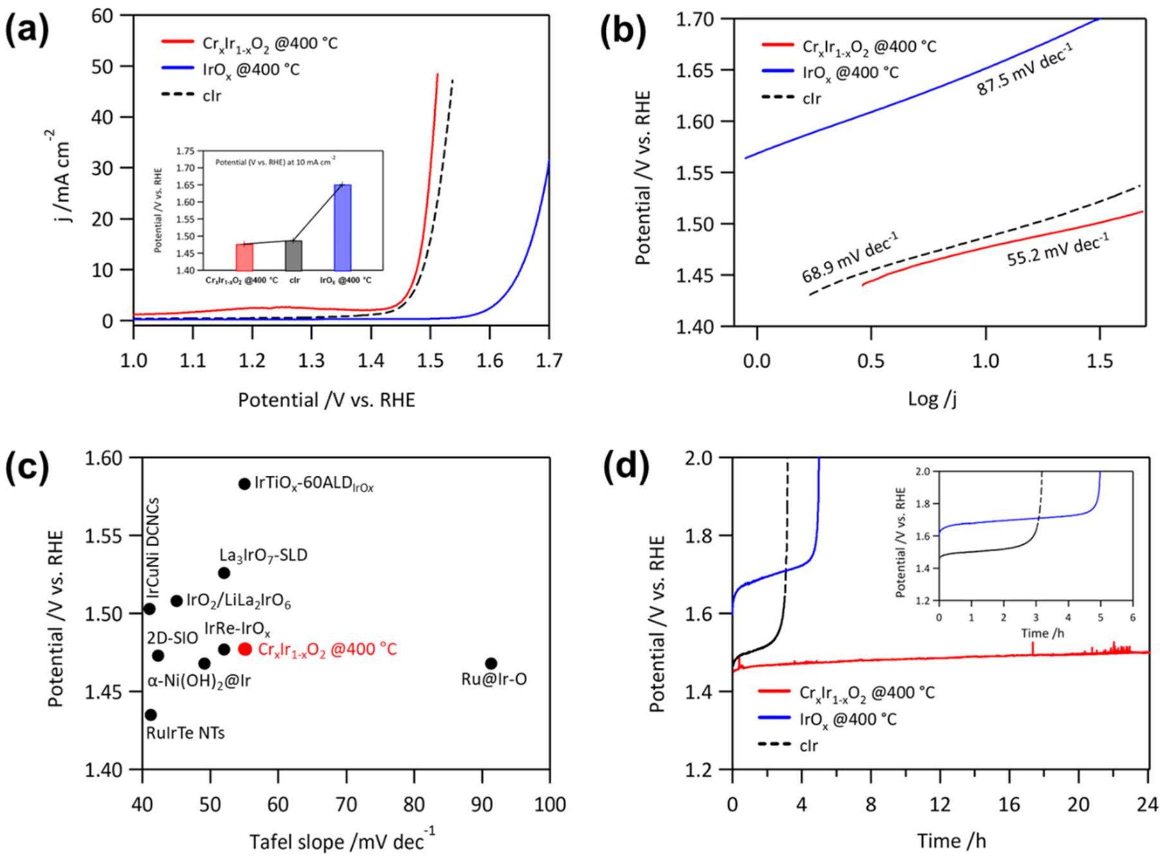

Fig. S8. Electrocatalytic OER measurements in 1.0 M H_2SO_4 (*aq*). (a) Polarization curves (current normalized by GSA) of the as-synthesized $Cr_xIr_{1-x}O_2$ @400 °C with IrO_x @400 °C and cIr as comparison. LVS polarization curves with RDE voltammetry were estimated with a rotating speed for 1600 rpm and a scan rate of 10 mV s^{-1}. Inset: comparison of potential at 10 mA cm^{-2} obtained from the Fig. S8(a). (b) Tafel plots derived from the LSVs recorded at 1 mV s^{-1}. (c) Comparison of Tafel slope and potential at 10 mA cm^{-2} in acidic electrolytes for $Cr_xIr_{1-x}O_2$ @400 °C and Ir-based catalysts with high OER performance in the literatures. The details for the samples and corresponding references are described in **Table S2**. (d) Chronopotentiometric performances of the samples under constant current density of 10 mA cm^{-2} for 24 h. Inset: chronopotentiometric response of wide range for time (*x*-axis).

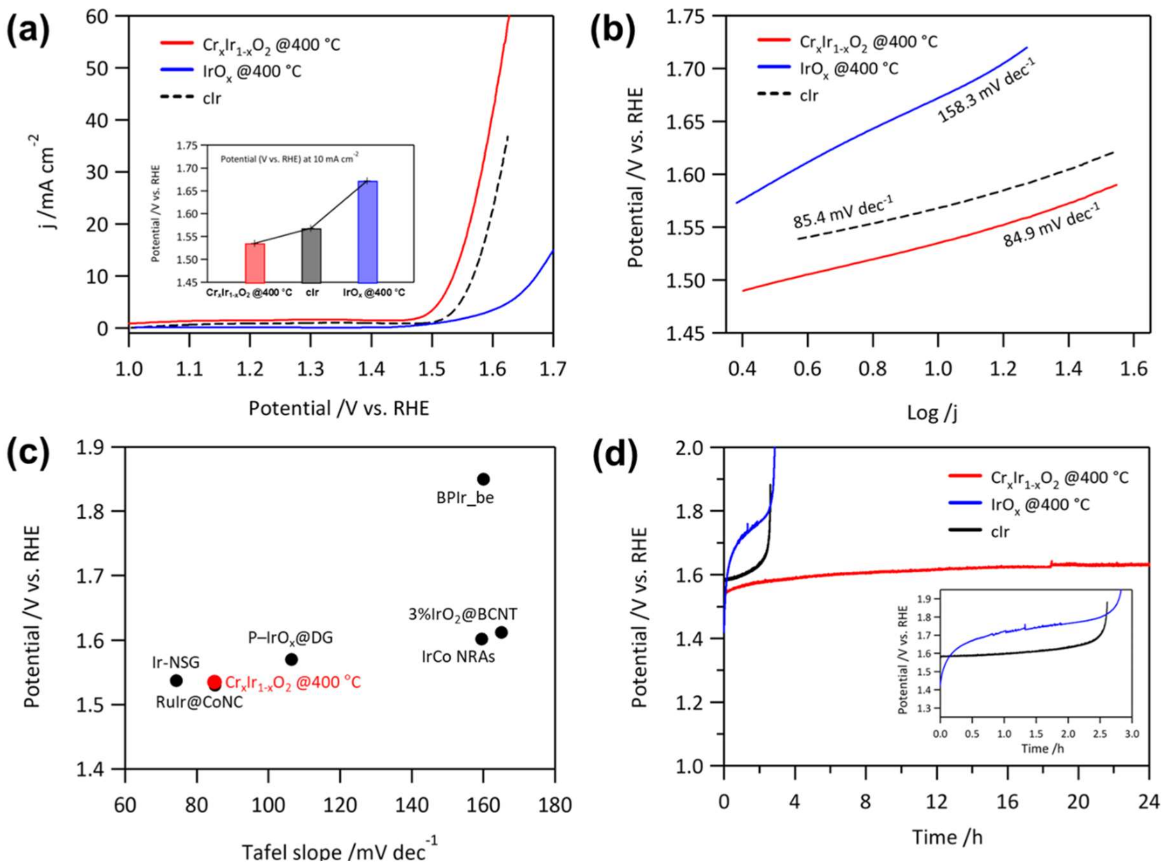

Fig. S9. Electrocatalytic OER measurements in 1.0 M PBS (*aq*, pH 7.4). (a) Polarization curves (current normalized by GSA) of the as-synthesized $Cr_xIr_{1-x}O_2$ @400 °C with IrO_x @400 °C and cIr as comparison. LVS polarization curves with RDE voltammetry were estimated with a rotating speed for 1600 rpm and a scan rate of 10 mV s^{-1}. Inset: comparison of potential at 10 mA cm^{-2} obtained from the Fig. S9(b). (b) Tafel plots derived from the LSVs recorded at 1 mV s^{-1}. (c) Comparison of Tafel slope and potential at 10 mA cm^{-2} in neutral electrolytes for $Cr_xIr_{1-x}O_2$ @400 °C and Ir-based catalysts with high OER performance in the literatures. The details for the samples and corresponding references are described in **Table S3**. (d) Chronopotentiometric performances of the samples under constant current density of 10 mA cm^{-2} for 24 h. Inset: chronopotentiometric response of wide range for time (*x*-axis).

Table S2. OER performances of $Cr_xIr_{1-x}O_2$ @400 °C and other previously reported Ir-based electrocatalysts in acidic media.

Catalyst	**Electrolyte**	**Potential @10 mA cm^{-2} (V *vs*. RHE)**	**Tafel slope (mV dec^{-1})**	**Reference**
$Cr_xIr_{1-x}O_2$ @400 °C	1.0 M H_2SO_4	1.477	55.2	This work
IrCuNi DCNCs	0.1 M $HClO_4$	1.503	41	Nano Lett. 2021, **21**, 7, 2809–2816
α-$Ni(OH)_2$@Ir	0.5 M H_2SO_4	1.468	49.1	Chem. Eng. J., 2021, **424**, 130337-130343
$IrO_2/LiLa_2IrO_6$	0.1 M $HClO_4$	1.508	45	J. Mater. Chem. A, 2022, **10**, 3393–3399
La_3IrO_7-SLD	0.1 M $HClO_4$	1.526	52	Adv. Energy Mater. 2021, **11**, 2003561-2003567
IrRe-IrO_x	0.1 M $HClO_4$	1.477	52	Electrochim. Acta, 2021, **398**, 139248-139256
RuIrTe NTs	0.5 M H_2SO_4	1.435	41.2	J. Mater. Chem. A, 2022, **10**, 2021–2026
2D-SIO	0.5 M H_2SO_4	1.473	42.3	J. Energy Chem., 2022, **66**, 619–627
Ru@Ir–O	0.5 M H_2SO_4	1.468	91.3	Small, 2022, **18**, 2108031-210838
$IrTiO_x$-60ALD_{IrOx}	0.5 M H_2SO_4	1.583	55	Adv. Mater. Interfaces 2022, **9**, 2102035-2102045

Table S3. OER performances of $Cr_xIr_{1-x}O_2$ @400 °C and other previously reported Ir-based electrocatalysts in neutral media.

Catalyst	**Electrolyte**	**Potential @10 mA cm^{-2} (V vs. RHE)**	**Tafel slope (mV dec^{-1})**	**Reference**
$Cr_xIr_{1-x}O_2$ @400 °C	1.0 M PBS (pH 7.4)	1.535	84.9	This work
RuIr@CoNC	PBS (Sigma-Aldrich, pH 7.2 ± 0.1)	1.53	85	ACS Catal. 2021, **11**, 3402–3413
BPIr_be	PBS	1.85	160	Adv. Mater. 2021, **33**, 2104638-210450
P–IrO_x@DG	1.0 M PBS	1.57	106.4	Small 2021, **17**, 2100121-2100128
IrCo NRAs	1.0 M PBS	1.6016	159.5	Chem. Eng. J., 2022, **433**, 133577-133584
3%IrO_2@BCNT	1.0 M PBS (pH 7.0)	1.612	165	Chem. Eng. J., 2021, **419**, 129567-129575
Ir-NSG	1.0 M PBS	1.537	74.2	Nat Commun, 2020, **11**, 4246-4255

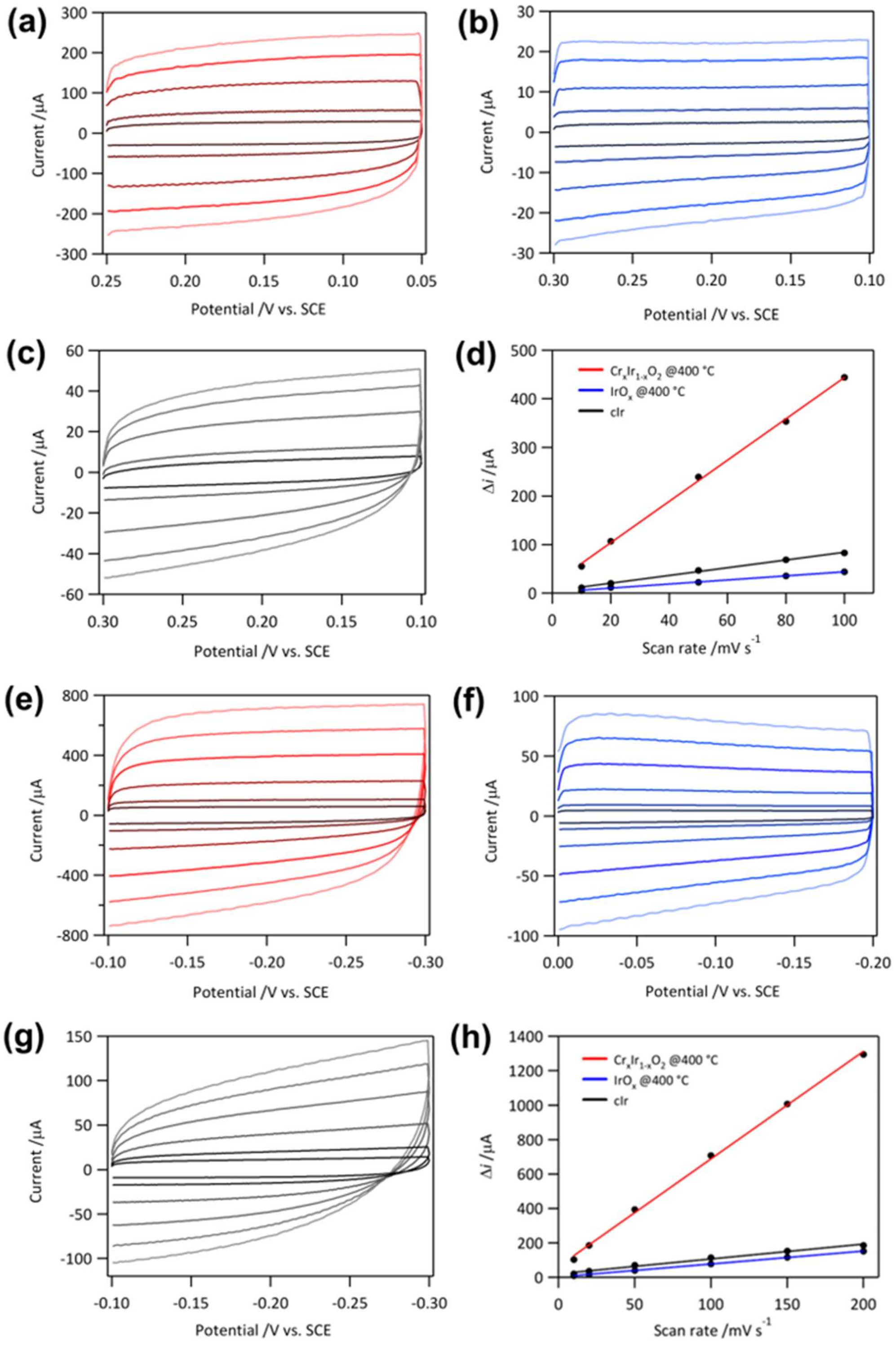

Fig. S10. Cyclic voltammograms of (a, e) $Cr_xIr_{1-x}O_2$ @400 °C, (b, f) IrO_x @400 °C and (c, g) cIr obtained in (a-c) 1.0 M H_2SO_4 and (e-g) 1.0 M PBS (pH 7.4) at various scan rates with a potential range of 0.2 V. Plots of Δ*i* (Δ*i* = cathodic current − anodic current at midpoint of potential range) *vs*. scan rate for the nanomaterials in (d) 1.0 M H_2SO_4 and (h) 1.0 M PBS, respectively.

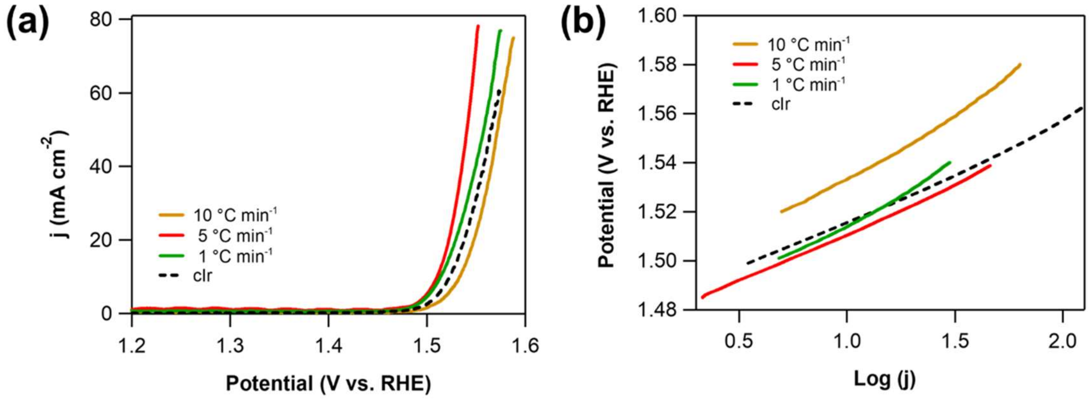

Fig. S11. (a) OER performance of Cr-Ir binary metal oxide alloys with different annealing speed condition (1, 5 and 10 °C min^{-1}) and cIr in the N_2-saturated 1.0 M KOH aqueous solution at a scan rate of 10 mV s^{-1} with rotating speed of 1600 rpm. (b) Tafel slopes of nanomaterials obtained from the RDE voltammograms shown in (a). Note that Tafel plots were derived from the LSVs recoded at 1 mV s^{-1}, and the sample annealed at a rate of 5 °C min^{-1} is identical with wire-in-tube nanofibers of $Cr_xIr_{1-x}O_2$ @400 °C.

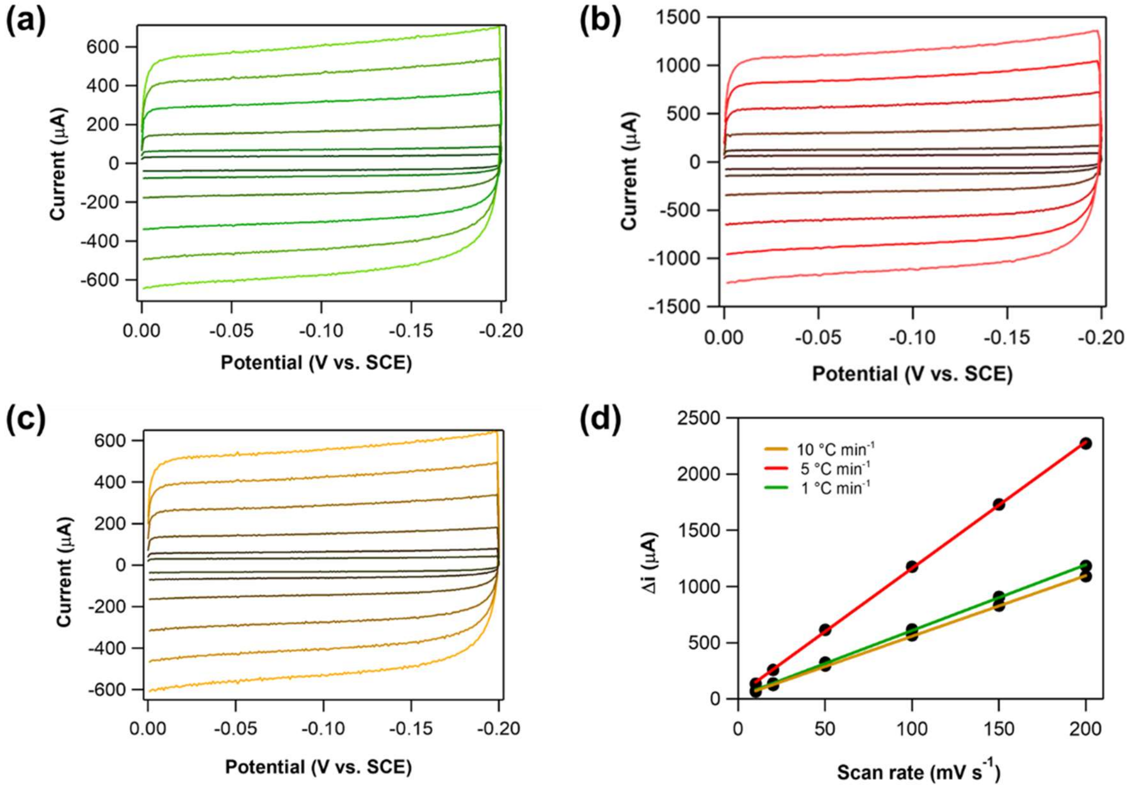

Fig. S12. Cyclic voltammograms of Cr-Ir binary metal oxide alloys annealed with (a) 1 °C min^{-1}, (b) 5 °C min^{-1} and (c) 10 °C min^{-1} obtained in 1.0 M KOH (*aq*) at various scan rates (10, 20, 50, 100, 150 and 200 mV s^{-1}) with a potential range of 0.2 V. (d) Plot of Δ*i* (Δ*i* = cathodic current − anodic current at -0.10 V) *vs*. scan rate for the nanomaterials. Note that the sample annealed at a rate of 5 °C min^{-1} is identical with wire-in-tube nanofibers of $Cr_xIr_{1-x}O_2$ @400 °C.

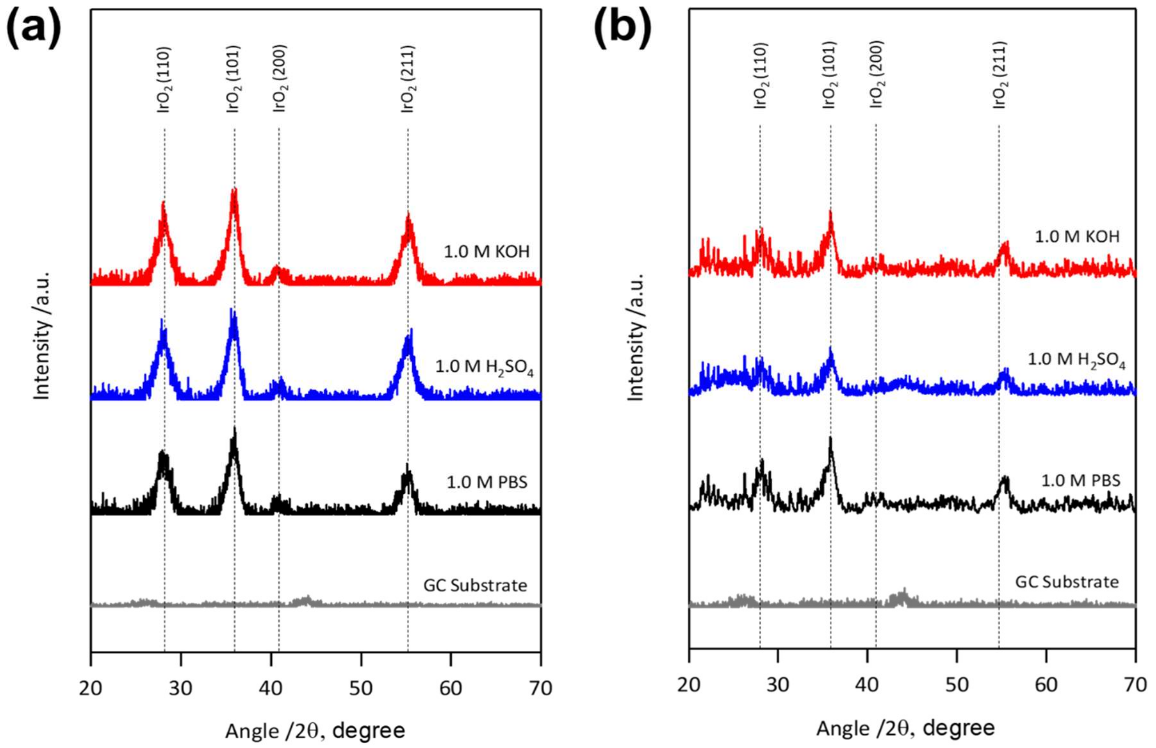

Fig. S13. XRD patterns of $Cr_xIr_{1-x}O_2$ @400 °C after the stability test for (a) 12 h and (b) 24 h under universal pH conditions (*i.e.*, 1.0 M KOH, 1.0 M H_2SO_4 and 1.0 M PBS), respectively.

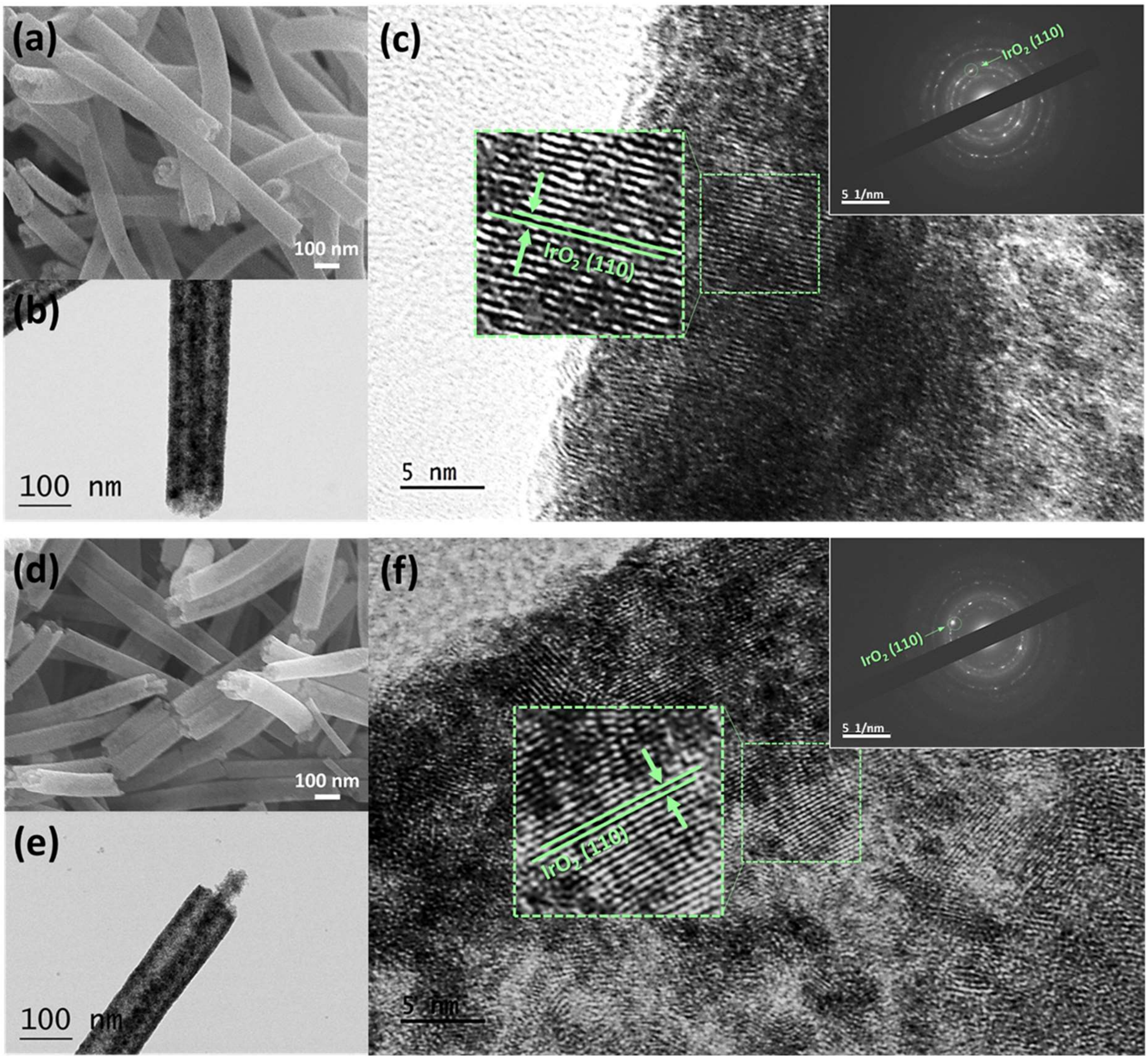

Fig. S14. Detailed crystal structures and morphological features of $Cr_xIr_{1-x}O_2$ @400 °C after stability test in 1.0 M KOH (*aq*) for (a-c) 12 h and (d-f) 24 h, respectively. (a, d) SEM images. (b, e) Low-magnification TEM images. (c, f) HRTEM images. Insets of (c, f) show SAED pattern of each nanomaterial.

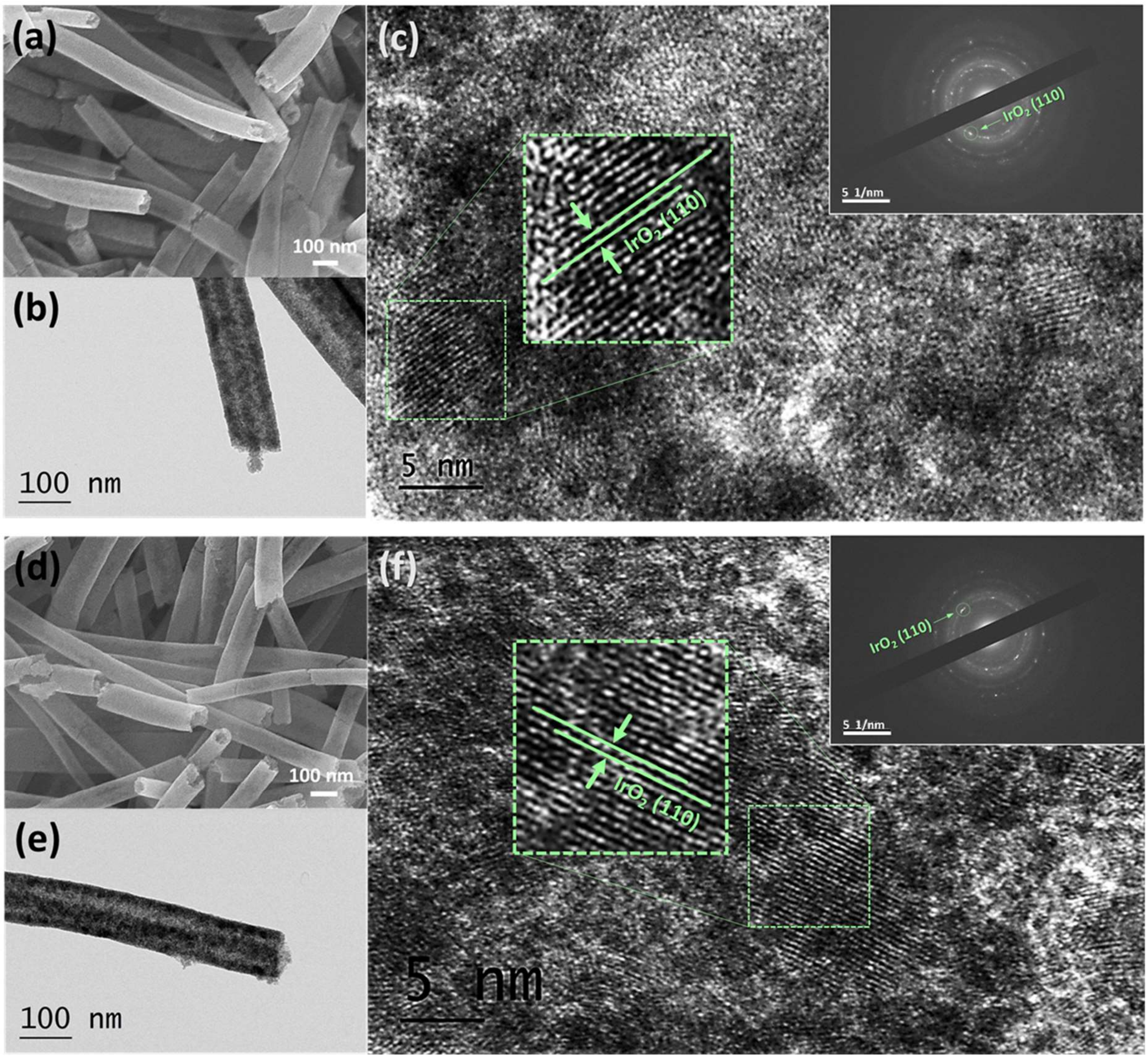

Fig. S15. Detailed crystal structures and morphological features of $Cr_xIr_{1-x}O_2$ @400 °C after stability test in 1.0 M H_2SO_4 (*aq*) for (a-c) 12 h and (d-f) 24 h, respectively. (a, d) SEM images. (b, e) Low-magnification TEM images. (c, f) HRTEM images. Insets of (c, f) show SAED pattern of each nanomaterial.

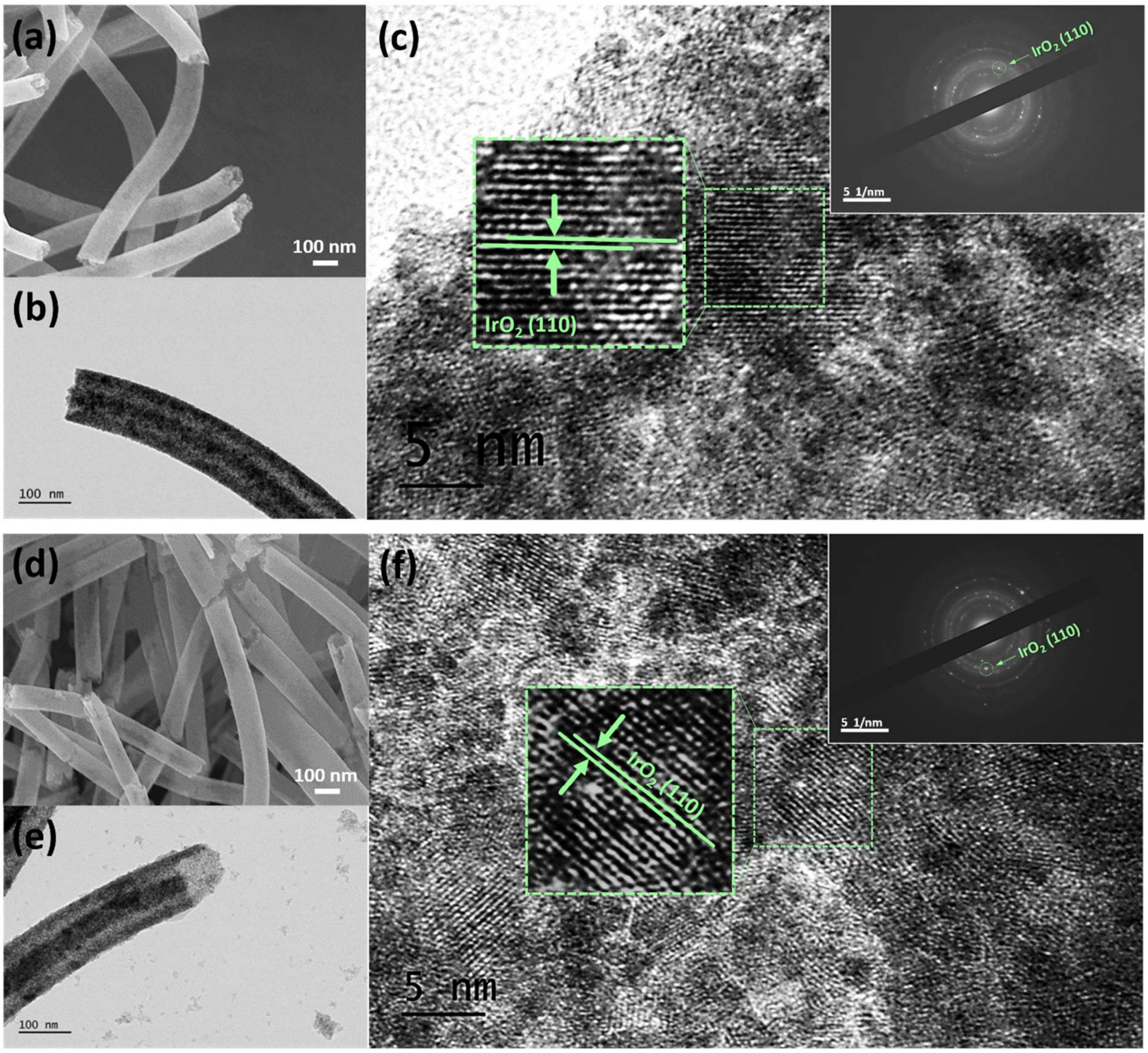

Fig. S16. Detailed crystal structures and morphological features of $Cr_xIr_{1-x}O_2$ @400 °C after stability test in 1.0 M PBS (*aq*, pH 7.4) for (a-c) 12 h and (d-f) 24 h, respectively. (a, d) SEM images. (b, e) Low-magnification TEM images. (c, f) HRTEM images. Insets of (c, f) show SAED pattern of each nanomaterial.

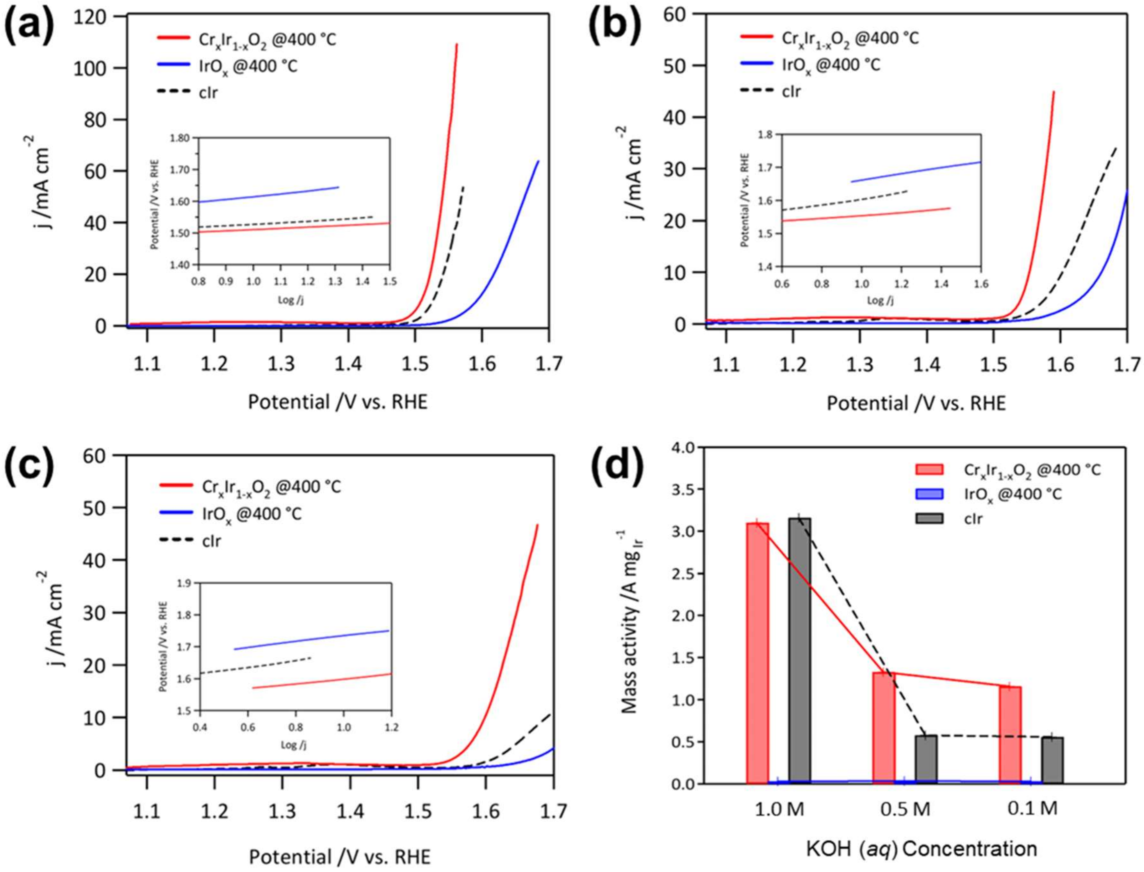

Fig. S17. (a-c) Polarization curves for OER in various KOH concentration with $Cr_xIr_{1-x}O_2$ @400 °C, IrO_x @400 °C and cIr as the electrocatalysts: (a) 1.0 M KOH, (b) 0.5 M KOH and (c) 0.1 M KOH. LVS polarization curves with RDE voltammetry were estimated with a rotating speed for 1600 rpm and a scan rate of 10 mV s^{-1}. Inset: Tafel plots derived from the LSVs recorded at 1 mV s^{-1}. (d) iridium mass activities (A mg_{Ir}^{-1}) in different alkaline concentration. Note, the mass activities are estimated using specific potentials for each concentration condition, respectively.

Table S4. Comparison of OER activities for $Cr_xIr_{1-x}O_2$ @400 °C, IrO_x @400 °C and cIr in various KOH concentration.

OER activities	KOH (*aq*) Concentration \ Sample	$Cr_xIr_{1-x}O_2$ @400 °C	IrO_x @400 °C	cIr
†Mass activity (A mg_{Ir}^{-1})	*1.0 M KOH	3.10	0.03	3.16
	**0.5 M KOH	1.33	0.03	0.58
	***0.1 M KOH	1.16	0.03	0.56
Potential at 10 mA cm^{-2} (V *vs*. RHE)	1.0 M KOH	1.510	1.591	1.523
	0.5 M KOH	1.553	1.661	1.603
	0.1 M KOH	1.598	1.735	1.690
Tafel slope (mV dec^{-1})	1.0 M KOH	39.3	78.4	47.9
	0.5 M KOH	43.3	90.0	88.9
	0.1 M KOH	76.2	90.3	98.5

†Mass activities were defined as OER activity normalized to the mass of Ir constituting nanomaterials (i.e., $Cr_xIr_{1-x}O_2$ @400 °C, IrO_x @400 °C and cIr) loaded on the working electrode.

*Mass activity was estimated at 1.560 V *vs*. RHE for all the samples.

**Mass activity was estimated at 1.590 V *vs*. RHE for all the samples.

***Mass activity was estimated at 1.660 V *vs*. RHE for all the samples.

Table S5. Formation energies of Cr_2O_3, IrO_2, and $Cr_{0.6}Ir_{0.4}O_2$.

Material	Formation energy (eV)	Number of atoms in the unit cell
Cr_2O_3	-5.184	Cr:16 / O:24
IrO_2	-4.822	Ir:16 / O:32
$Cr_{0.6}Ir_{0.4}O_2$	-4.399	Cr:10 / Ir: 6 / O:32

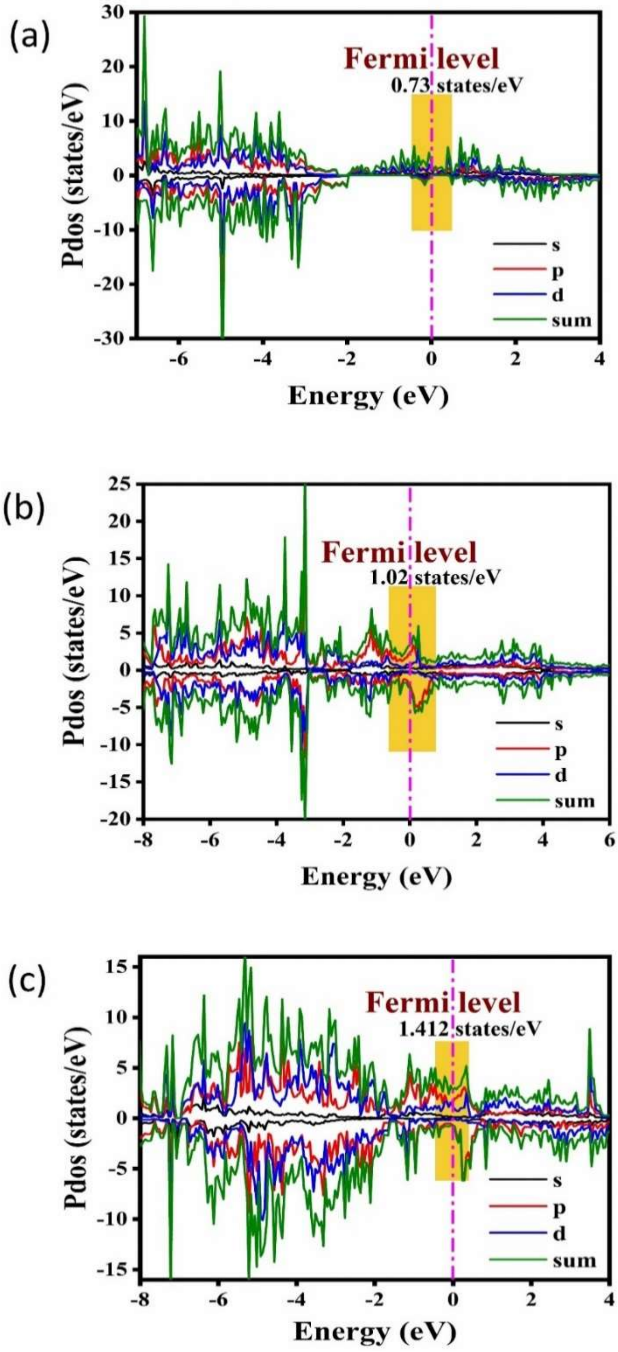

Fig. S18. Partial Density of states for the catalyst of, (a) Cr_2O_3, (b) IrO_2, and (c) $Cr_{0.6}Ir_{0.4}O_2$.

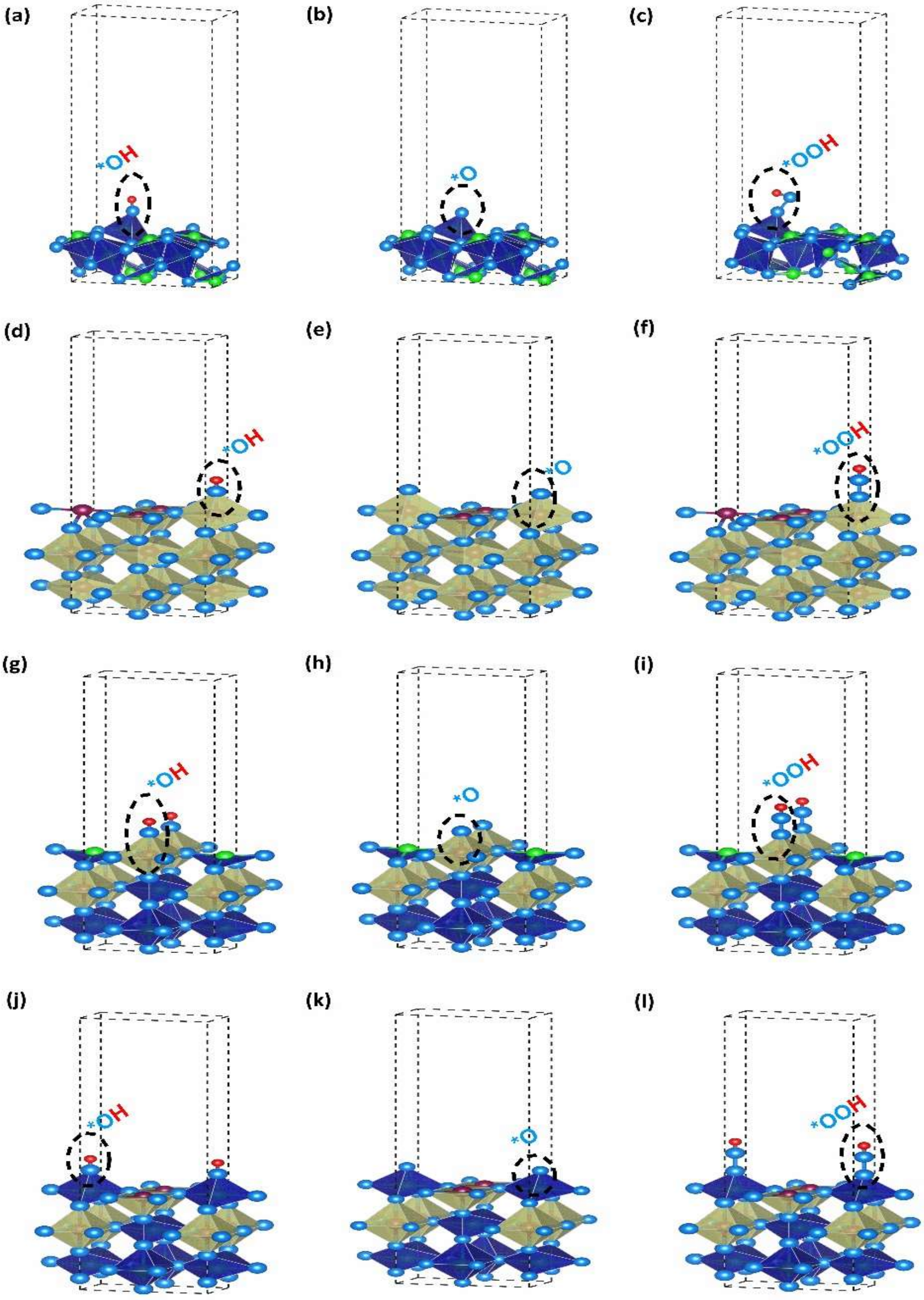

Fig. S19. OH, O and OOH adsorption on active sites of (110) surfaces; (a-c) $*Cr_2O_3$, (d-f) $*IrO_2$, (g-i) $*Cr_{0.6}Ir_{0.4}O_2$, and (j-l) $Cr_{0.6}*Ir_{0.4}O_2$. * Denotes active site. Color representation: green- chromium, brown- iridium, blue-oxygen, and red-hydrogen.

Table S6. Gibbs free energy values and OER overpotentials of the active catalyst sites on (110) surfaces.

Material	Adsorption site	Gibbs free energy change (eV)				OER Overpotential (η, V)
		ΔG_1	ΔG_2	ΔG_3	ΔG_4	
Cr_2O_3	Cr	-0.552	0.742	1.621	3.109	1.88
IrO_2	Ir	0.746	0.918	1.680	1.576	0.45
$Cr_{0.6}Ir_{0.4}O_2$	Cr	0.793	1.539	1.201	1.387	0.31
	Ir	1.503	1.448	1.603	0.366	0.37

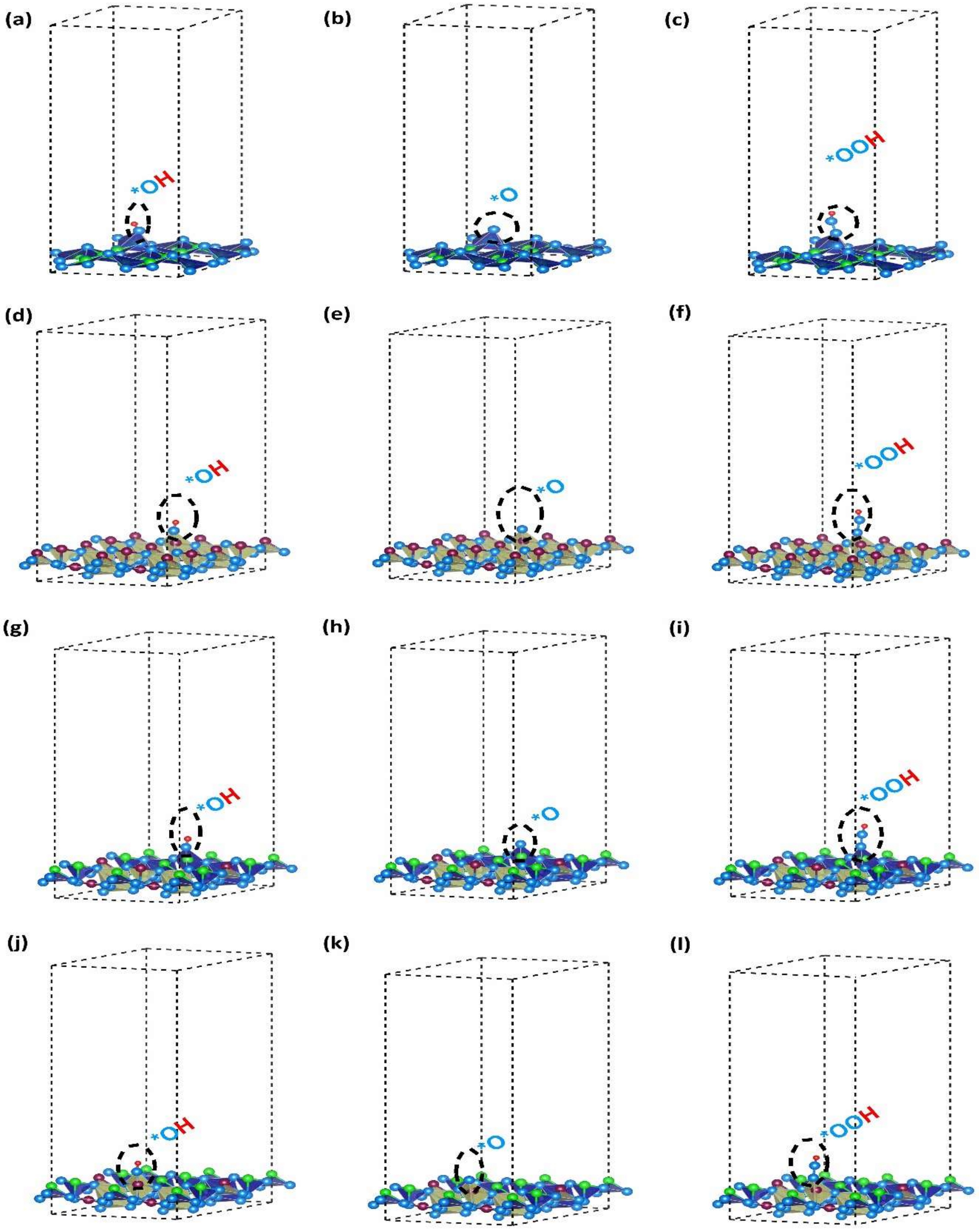

Fig. S20. OH, O and OOH adsorption on active sites of (211) surfaces; (a-c) $^*Cr_2O_3$, (d-f) $^*IrO_2$, (g-i) $^*Cr_{0.6}Ir_{0.4}O_2$, and (j-l) $Cr_{0.6}{}^*Ir_{0.4}O_2$. * Denotes active site.

Table S7. Gibbs free energy values and OER overpotentials of the active catalyst sites on (211) surfaces.

Material	Adsorption site	Gibbs free energy change (eV)				OER Overpotential (η, V)
		ΔG_1	ΔG_2	ΔG_3	ΔG_4	
Cr_2O_3	Cr	2.216	1.302	1.729	-0.327	0.99
IrO_2	Ir	1.746	0.734	1.657	0.783	0.52
$Cr_{0.6}Ir_{0.4}O_2$	Cr	-0.732	1.414	1.595	2.643	1.41
	Ir	0.741	1.661	1.617	0.901	0.43